ANALYSIS OF AERODYNAMIC INTERFERENCE CHARACTERISTICS AND AEROACOUSTICS FOR HIGH-SPEED COMPOSITE HELICOPTER IN HOVER

L.-Y. Huang[1], X. Zhao[1], X.-C. Li[1]

[1]School of Aeronautics, Northwestern Polytechnical University, Xi'an, Shaanxi, 710072, China

Abstract

The special configuration of rotor, fixed wing and thrust propellers is employed in the X3 high-speed composite helicopter to achieve Vertical Take-off and Landing (VTOL) and high-speed cruise capability. The wing is in the rotor downwash, resulting in negative wing lift and increased rotor thrust. The propellers on both sides of the wing produce opposite thrust to balance the counter torque of the rotor, and the thrust magnitude is related to the hovering attitude. At the same time, the rotor/propeller/fuselage aerodynamic interference constitutes the unique aerodynamic noise characteristics of the helicopter.

To investigate the aerodynamic interference of rotor/propeller/wing and space noise distribution, firstly, the quasi-steady flow models with medium precision were used to evaluate the isolated rotor and propeller performance quickly. Then the fast algorithm for aerodynamic trim of composite helicopters was applied with control parameters and attitude parameters determined. After that, the unsteady flow models with high precision were used to predict the components performance under flow interference around the whole helicopter flow field. Finally, based on the FW-H equation of permeable surface and IDDES model, the whole helicopter noise was predicted in hover.

To validate the simulation model, Robin helicopter was used as a benchmark for rotor/fuselage interference. The UH-1H rotor was used to verify noise performance in hover condition, and the SR-2 propeller was used to verify discrete noise characteristics. The calculated results were agreed well with the experimental data. Based on verification,the whole flow field of the helicopter was simulated that, the wing had a blocking effect on the rotor downwash flow, the left and right propeller slip flow deflected due to the influence of the rotor downwash flow, and the spatial distribution and noise level of the whole helicopter was affected by the tip vortex interference between the rotor and the fuselage/propeller

Keywords: Compound high-speed helicopter, Aerodynamic interference, Unsteady flow, Acoustic

1. Introduction

The compound high-speed helicopter, represented by the X3 configuration, uses a thrust propeller structure, due to the fixed wing and propeller configuration, most drag could be overcome by the thrust propeller, reducing the forward flight resistance caused by the rotor disk and fuselage forward tilt [1]. The configuration has a maximum flight speed of 463km/h and a cruising speed of 407km/h [2]. However, this special arrangement can cause serious interference among the rotors, propellers and wings, which would affect the aerodynamic characteristics of the rotor, propeller and wing, and bring difficulties to the flight control [3]. At the same time, the rotor and propellers wake interact with the fuselage simultaneously, forming the unique acoustic characteristics of the helicopter. Therefore, it is of great significance to study the flow interference of rotor/propeller/wing and predict their effect on the change of helicopter aerodynamic and acoustic characteristics for the special configuration.

Figure 1 – X3 configuration compound high-speed helicopter

In the study of the flow field interference between the complex power blade and the whole helicopter, the commonly used numerical methods are: Momentum source method [4][5][6][7], unsteady panel/viscous vortex particle hybrid method [8][9], time-step full-span free-wake method [10] and quasi-steady and unsteady flow simulation method etc. The rotating coordinate system is adopted for propellers and rotors, and the flow is considered to be steady approximately. The instantaneous action is ignored. It provides a more accurate flow field characteristics than the momentum source method, which is often used for the aerodynamic calculation of a single rotating blade. Chen, et al [11] used the Moving Reference Frame(MRF) method combined with N-S equation to show that the flow phenomenon conforms to the characteristics of propeller flow, and the interference to aircraft aerodynamic performance was well simulated. Furthermore, the sliding or overset mesh method are employed for the unsteady simulation method to reflect the characteristics of bidirectional flow interference and unsteady flow between the rotating blade and other components. It is widely used to predict aerodynamic characteristics, load distribution and pressure fluctuation of helicopter com-ponents. But the calculation amount and calculation cost are large. In Sliding Mesh(S-M) [12] method, the computing domain is divided into dynamic and static regions, which are connected by the sliding transfer interface. The dynamic grid moves along the interface as a whole, and the flux transfer is realized through the information interpolation between nodes.

In this paper, a helicopter model with X3 configuration is designed, the geometry and working conditions of wing, rotor and propellers are determined. Then the quasi-steady flow simulation method was used to predict the aerodynamic characteristics of rotor and propeller at different collective pitch. Combined with the helicopter trim program, the working parameters of the helicopter were determined in hover. Then the unsteady flow simulation method was used to predict the aerodynamic characteristics of rotor, propeller and wing in the whole helicopter flow field. Finally, the spatial distribution of the whole helicopter acoustic was predicted and analyzed combined with the flow interference in hover.

1.1 The Aerodynamic Design of Compound Helicopter

Since the X3 composite helicopter was based on the AS365N Dauphine fuselage, the geometric parameters of the proposed configuration were obtained by referring to the shape characteristics of the helicopter. Figure 1 shows the three views of the model. And the overall parameters of X3 configuration helicopter are shown in Table 1.

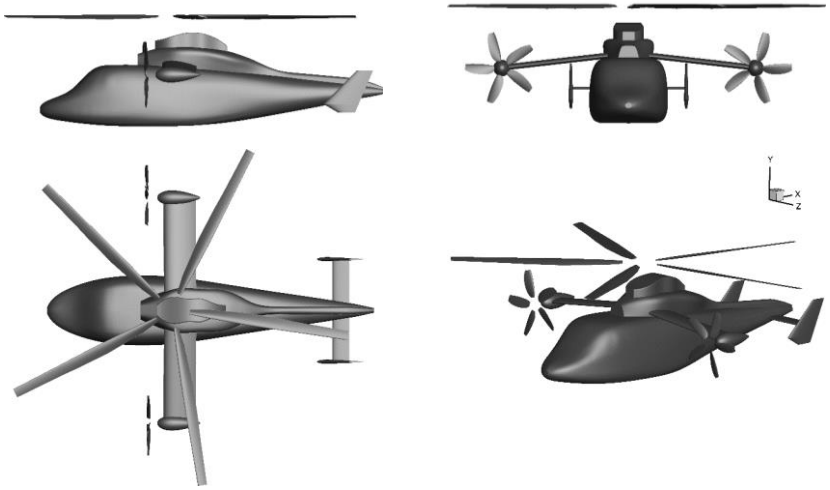

Figure 2 – The X3 helicopter model in three views and stereogram

Table 1 – General parameters of the composite helicopter

Parameter	Value
Total length /m	10.11
Total width /m	10.97
Total height /m	3.228
Wingspan /m	7
Wing chord /m	1
Wing airfoil	NACA4415
Weight /kg	5200
Power /kw	1693

The geometry of XH-59A main rotor blade is adopted but changed to 5 pieces in the model. Other parameters are established referring [13-14]. Table 2 shows the parameters of the main rotor.

Table 2 – Main rotor parameters

Parameter	Value	Parameter	Value
Rotor radius /m	5.485	Direction of rotation	Dextrorotation
Chord length /m	0.286	Number of blades	5
Rotation speed /rpm	344.83	Airfoil profile	NACA0026&
Negative twist /°	-9.5		NACA632xxA

With reference to [15], propeller parameters were obtained and shown in Table 3. The chord length and twist angle distribution of the propeller is shown in Fig. 2.

Table 3 – Propeller parameters

Parameter	Left	Right
Radius /m	1	1
Root cut /m	0.2	0.2
Number of blades	5	5
Airfoil	Clark-Y	Clark-Y
Chord length /m	0.28	0.28
Negative twist /°	-23	-23
Rotate speed /rpm	2200	2200
Direction of rotation	Levorotation	Dextrorotation
Distance between propeller Shaft and fuselage axis /m	3.5	3.5

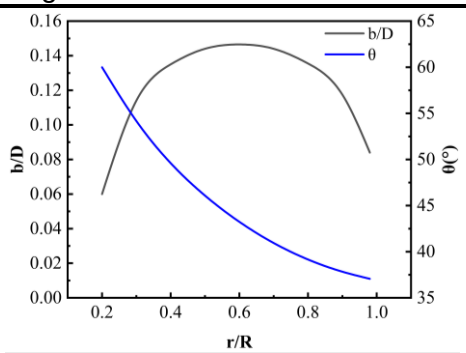

Figure 3 – The chord length and angle distribution of the propeller

With reference to [16], wing parameters were obtained and shown in Table 4.

Table 4 – Wing parameters

Parameter	Value
Wingspan /m	7
Chord length /m	1
Area /m2	7
Aspect ratio	7
Setting Angle /°	6

Dihedral angle /°	-4
Airfoil	NACA4415
Airfoil lifting-line slope	5.73
Ratio of aileron to wing area	6%

Referring [17], parameters were obtained and shown in Table 5.

Table 5 – Horizontal tail parameters

Parameter	Value
Wingspan /m	3.2
Chord length /m	0.52
Area /m2	1.664
Setting Angle /°	-1
Airfoil	NACA4415
Airfoil lifting-line slope	5.73
Ratio of elevator to horizontal tail area	30%

1.2 Noise Equation

This paper employed the FW-H equation to specify the sound generation equation of the control surface moving arbitrarily in the fluid field [18], see equation (1):

$$\begin{aligned}\left(\frac{1}{c^2}\frac{\partial^2}{\partial t^2}-\frac{\partial^2}{\partial {x_i}^2}\right)p'(x_i,t)&\\ =\frac{\bar{\partial}}{\partial t}\{[\rho_\infty v_n+\rho(u_n-v_n)]\delta(g)\}&\\ -\frac{\bar{\partial}}{\partial x_i}\{[-\boldsymbol{P}'_{ij}\cdot\boldsymbol{n}'_j+\rho\boldsymbol{u}_i(u_n-v_n)]\delta(g)\}&\\ +\frac{\bar{\partial}^2}{\partial x_i x_j}[(-\boldsymbol{P}'_{ij}+\rho\boldsymbol{u}_i\boldsymbol{u}_j-c^2\rho'\delta_{ij})\cdot H(g)]&\end{aligned} \tag{1}$$

Where c, $\boldsymbol{u}_i$ and $\boldsymbol{u}_j$, $\boldsymbol{P}'_{ij}$ are the sound velocity, velocity components, and stress tensor, respectively. $p'(x_i,t)$ is the sound pressure intensity value of the observation point x_i at time t. δ_{ij} is Kronecker symbol. The subscript "∞" represents the undisturbed item, the superscript "$'$" represents the disturbed item. The subscript "n" represents the projection in the normal direction outside the control surface. $\bar{\partial}$ is the generalized derivative, $H(g)$ is the Heaviside function, and $\delta(g)$ is the Dirac function.

For the unsteady flow of rotors, the non-rotating interface is selected as the penetrable sound source surface, the thickness noise, loading noise, and quadrupole noise can be calculated. For the quasi-steady flow of the rotor, the blade surface is selected as the impenetrable sound source surface, only the thickness noise and loading noise can be considered.

Using Fast Fourier Transform (FFT), the Sound Pressure Level (SPL) can be calculated in equation (2)

$$L_p=10\lg(\frac{\tilde{p}}{p_{ref}})^2=20\lg(\frac{\tilde{p}}{p_{ref}}) \tag{2}$$

Where L_p is SPL, which is measured in decibels (dB); and $p_{ref}=2\times10^{-5}$ Pa.

2. Verification and aerodynamic performance prediction of the isolated main rotor and propellers

2.1 Verification of Flow Interference between Rotor and Fuselage

The experimental data of flow interaction between rotor and fuselage of Robin helicopter at advance ratio 0.01[19] is selected as the validation. The scaled 2-meter rotor test system is employed. It consists of four rectangular blades with radius 0.861m.

The blade is composed of NACA 0012 airfoil with a radius 0.861m. It has a chord length 0.0663m

and linear torsion angle is -8°, rotating at 2000rpm. The length of the fuselage is 2m, and the distance between the hub and the center of the fuselage is 0.322m. In the test, the cyclic pitches are -0.1° and 0.2° .Considering they are much less than 1° , therefore, cyclic pitches are ignored in the simulation. Steady flow simulation is carried out using Moving Reference Frame (MRF) method, and the spatial discretization second-order scheme were used.

According to the collective pitch 9.4° , shaft angle 0° and rotating speed, a cylindrical rotational domain surrounding the rotor was created. And the stational domain surrounding the fuselage was built, which is a sphere with 25 times the rotor radius surrounds the helicopter. Both domains employ unstructured mesh. The total number of grids of the former is 6.8 million with the first layer mesh thickness 1×10^{-5}m, and 2.1 million for the latter. Fig. 4 shows the grid distribution on the plane of the rotor and on surface of the blade. Fig. 5 reveals the grid on the surface of the fuselage.

The papers should be prepared, if possible, using the format like this document.

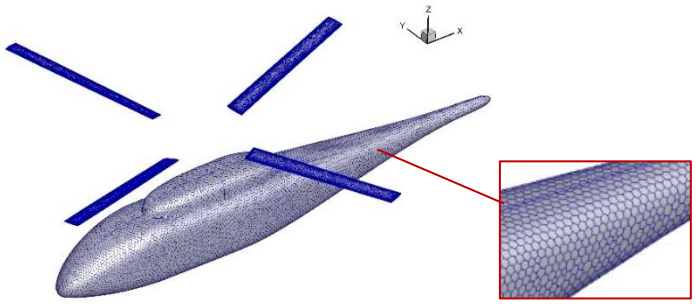

Figure 4 – Mesh distribution on the surface of fuselage and rotor

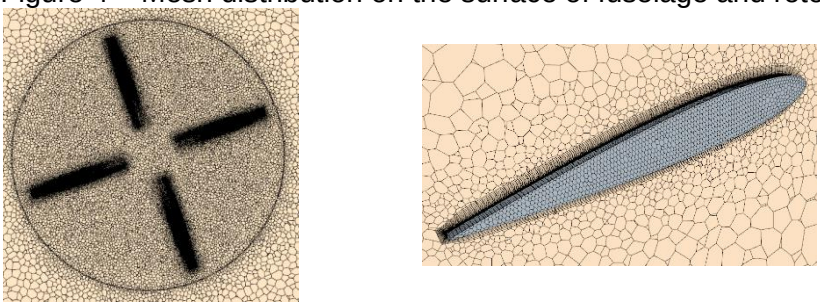

Figure 5 – Mesh distribution on rotor plane and surface

The far-field boundary condition is employed for the sphere, and moving reference frame method is applied for the rotating domain. The calculated thrust coefficient ratio to solidity is 0.044, which has 7.31 % error compared to the experimental result.

The monitoring point y=0.007 near the symmetry axis of the fuselage is selected to correspond to the distribution position of the experimental sensor, as shown in the figure 6. X/L in the figure 7 is defined as the ratio of the cross-section coordinates along the fuselage to the fuselage reference length, and the expression Cp of the fuselage surface pressure coefficient is as follows:

$$C_p \times \frac{2}{\mu^2} = \frac{P - P_\infty}{\frac{1}{2}\rho_\infty V_\infty^2} \tag{3}$$

Where: μ denotes the advance ratio of the rotor.

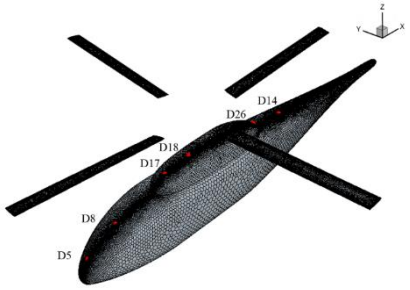

Figure 6 – Mesh distribution on rotor plane and surface

Figure 7 shows the pressure coefficient distribution at the corresponding monitoring point. The variable course of the unsteady pressure at each monitoring point with the azimuth Angle presents a 4Ω periodic characteristic, which is mainly manifested by the influence of blade passage. The

unsteady method fits the peak phase well, and the maximum error between the tension coefficient and the experimental value is 7.1%. It shows that the numerical method established in this paper is more accurate to simulate the rotor fuselage interference and can be used to calculate the rotor/fuselage interference.

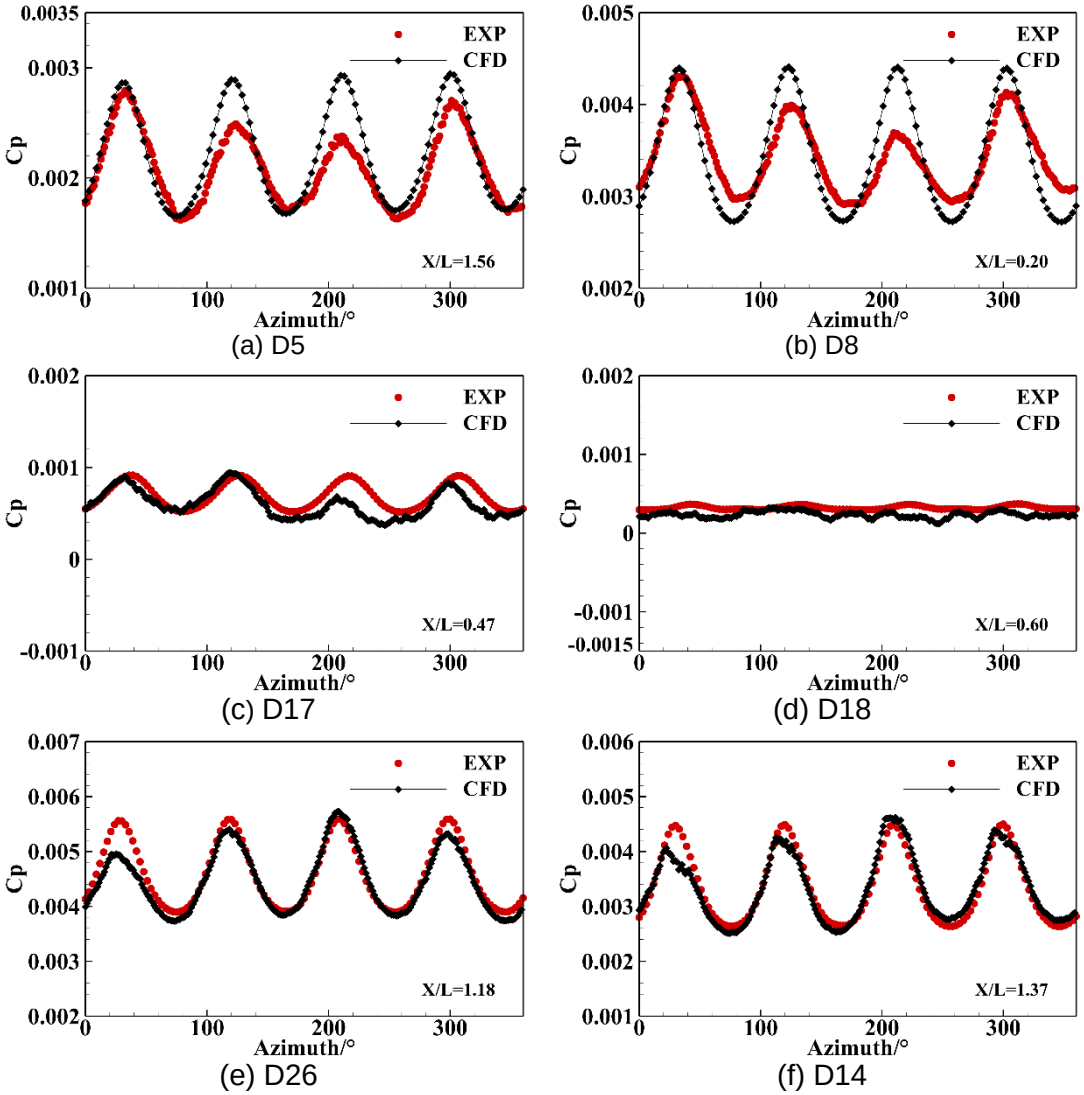

(a) D5 (b) D8 (c) D17 (d) D18 (e) D26 (f) D14

Figure 7 – The unsteady pressure change history of each sensor in the ROBIN body

2.2 Verification of Rotor Aerodynamic and Acoustic

The UH-1H two-blade rotor model was used to verify the noise performance of rotor in hover. The rotor parameters were shown in Table 6 [20].

Table 6 – UH-1H rotor parameters

Parameter	Value	Parameter	Value
Radius /m	1.045	Airfoil	NACA0012
Chord length /m	0.0762	Tip Mach number	0.85
Aspect Ratio	13.71	collective pitch/°	0
Number of blades	2	Blade plane profile	rectangle
Grids number(steady) /million	1.26	Grids number(unsteady) /million	6.35

The shape of the device is simplified in numerical simulation, ignoring the influence of the hub and connecting rod in the device. The distance between the noise observation point and the center of the rotor rotation plane is 3.09R， as shown in Figure 8 . The trend of sound pressure of UH-1H rotor with time was calculated under the condition of collective pitch Angle θ = 0° (i.e., no lift) and tip Mach number $Ma\omega R$ = 0.85.

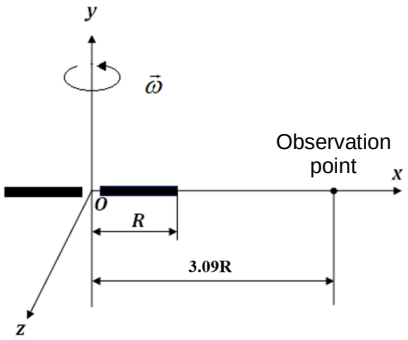

Figure 8 – Observation point of UH-1H rotor hover noise experiment

The results of quasi-steady and unsteady sound pressure calculation are compared with the experimental data in Table 7. The results show that the unsteady method is accurate and effective to predict noise. The error of quasi-steady method is larger because only linear noise including thickness noise and load noise is considered. It can be seen from the Figure 9 that the time-domain phase calculated by the two methods is in good agreement with the test values. In terms of the negative peak value of noise, the error between the unsteady method and the experiment is only 1.9Pa. It is shown that FW-Hpds equation based on permeable surface can be used to calculate rotor noise including quadrupole noise.

Table 7 – Comparison of calculation results

	Quasi-steady	Unsteady
RMSE /Pa	19.75	4.54
Negative peak noise error /Pa	51.2	1.9

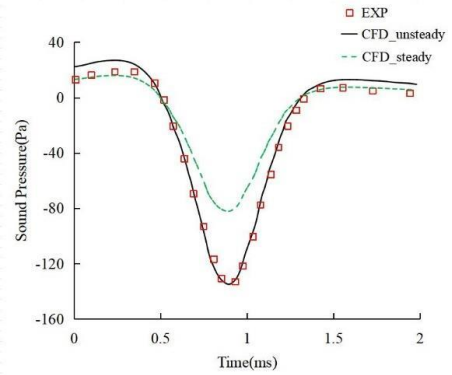

Figure 9 – Comparison between experimental and calculated values of UH-1H rotor noise in hover

2.3 Verification of Propeller Aerodynamic and Acoustic

This experiment was performed by Paul Soderman and W. Clifton Horne in the NASA AMES Research Center 7-by-10 foot wind tunnel in 1990, in a study of aerodynamic and acoustic results of a pusher propeller [21]. The purpose of the experiment was to measure detailed wake and noise properties from a 591 mm SR-2 propeller, particularly when the pusher propeller is operating in the wake of an I-tail, Y-tail, and V-tail empennage. The experimental conditions selected for validation as shown in Table 8.

Table 8 – Experiment Conditions for SR-2 in Low Speed Condition

Parameter	Value
Diameter /m	0.591
Number of blades	4
Mach number	0.18
Blade pitch angle /°	21
Rotate speed /rpm	8200
Helical Tip Mach number	0.76

The propeller utilized, the NASA SR-2 scaled propeller, is an unswept propeller consisting of NACA

65 series airfoils from the propeller root through to 37% percent of the blade radius, followed by a transition region to NACA 16 series airfoils, which define the propeller section from 44% of the radius to the propeller tip. This geometry is described in Fig. 10. Acoustic measurements were made via 13 transducers, Fig. 11.

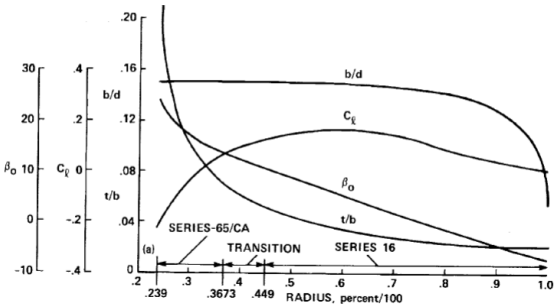

Figure 10 – SR-2 Propeller Geometry, describing (a) spanwise distribution of chord (b), twist (β_0), thickness (t), diameter (d), and design lift coefficient (C_ℓ) [21]

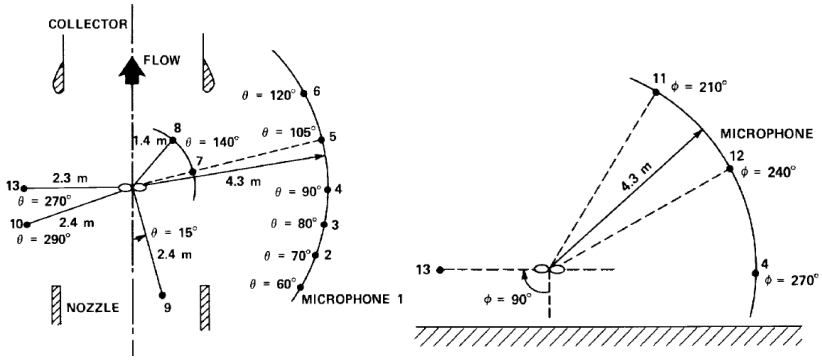

Figure 11 – Transducer locations relative to the propeller hub, overhead perspective (left) and the plane containing the propeller looking downstream (right) [21].

Using unstructured polyhedral mesh, the stationary and rotating domains are constructed with the center of the propeller disk plane as the origin. The stationary domain chosen consists of a cylinder extending a distance of 10 diameters in the radial direction, 11 diameters upstream and 21.5 diameters downstream from the propeller. The rotating cylinder has a diameter of 0.8 m (135% of the propeller diameter), extending 0.2 m upstream and 0.4 m downstream of the propeller. The far-field boundary is free incoming flow with Mach number 0.18. The number of rotating domain grids was 23.7 million, with the first layer mesh thickness 2.79×10^{-6} m, and the grid in the static domain was 1.12millon.

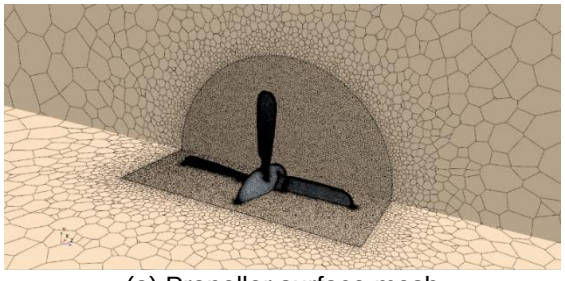

(a) Propeller surface mesh

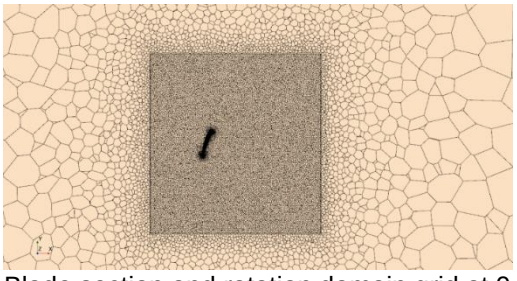

(b) Blade section and rotation domain grid at 0.7R

Figure 12 – Propeller mesh

Unsteady flow simulation is carried out using sliding mesh technology. The third-order MUSCL scheme is adopted for space discretization, and the 2nd order scheme is adopted for time discretization. The IDDES model is employed. Time step size is 1°, with 10 internal iterations. Relative definitions are presented in equation (4)~(5)：

$$C_{T_p} = \frac{T_p}{\rho n_s^{\,2} D^4} \tag{4}$$

$$C_{Pp} = \frac{P_p}{\rho n_s^{\,3} D^5} \tag{5}$$

Table 9 – Aerodynamic performance of unsteady flow model

	Thrust	Torque	CT	CP
EXP	224.93	21.586	0.083	0.086
Unsteady	191.19	17.71	0.071	0.069
error			15.00%	17.96%

As can be seen from the table 9, there are some errors between the tension coefficient and torque coefficient obtained by the unsteady method and the experiment, and the error is less than 20%. The main reasons for the error are: 1. The airfoil used in modeling was different from the airfoil provided in the literature, resulting in the appearance error between the model and the real propeller; 2. The size of the non-structural polyhedral mesh used was unreasonable and needs to be further improved; 3. The setting condition of the solver was different from the real condition; 4. The full turbulence model was used, which is different from the actual flow, resulting in aerodynamic prediction errors.
The unsteady method was used to solve the convergent flow field, and the FW-H equation based on the penetrating surface was used to predict the propeller noise. The interface of the outer side of the rotating region was selected as the permeable surface, and the results were read after 8 revolutions of the propeller. The sound pressure level pairs of fundamental frequency and double frequency at the receiving point are shown in the table 10.

Table 10 – Blade Passage Frequency Noise Predictions for SR-2

	BPF	Frequency (Hz)	Experimental Data(dB)	CFD(dB)	Error
Receiving point 7	1	547	101	102.13	1.13
	2	1093	94	94.54	0.54
	3	1640	88	86.7	-1.30
	4	2187	81	78.74	-2.26
	5	2733	76	74.31	-1.69
Receiving point 8	1	547	87	88.13	1.13
Receiving point 12	1	547	101	96.75	-4.25
	2	1093	96	89.19	-6.81
	3	1640	91	83.21	-7.79
	4	2187	83	76.99	-6.01
	5	2733	77	70.32	-6.68

Note: The spectrum diagram of discrete noise and sound pressure level at receiving point 7 and 12 was provided only, and the fundamental sound pressure level at receiving point 8 is provided only. The key results to predict are the magnitudes of the Blade Passage Frequencies (BPFs), which define peak noise values for propellers. The table 11 shows that the receiving point 7 error is small, the sound pressure level error range is -2.26~1.13(dB), and the receiving point 12 error is larger. FIG. 13 shows the basic frequency sound pressure level of the propeller at the receiving points 7, 8 and 12 compared with the experiment. It can be seen that the sound pressure level errors at the fundamental frequency positions 7 and 8 are all less than 12 points.

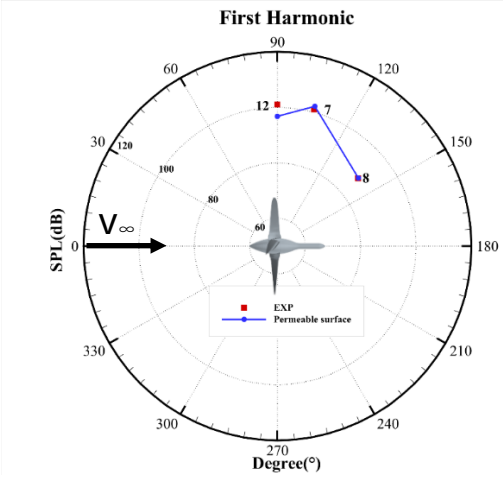

Figure 13 – First harmonic acoustic results (SPL)

The figure 14 shows the sound pressure level spectrum of receiving points 7 and 12 compared with

the experiment, along with measurements of ambient wind tunnel spectra for the wind tunnel for receiving point 7. It can be seen from the figure that CFD is more accurate in capturing the frequency of the propeller blade, and the peaks corresponding to the fundamental frequency and 2-3 octave frequency are in good agreement with the experiment. The CFD value is closer to the sound pressure level measured by experiment at the receiving point 7, but slightly lower than the experimental value at the receiving point 12, as shown in Table 11. At the same time, Figure 14 also shows that the background noise of the experiment is relatively large, because the experiment is not carried out in an acoustic wind tunnel; In addition, in the experiment, silencer plates were arranged near the microphone on the horizontal plane of the propeller shaft to reduce the wall reflection noise, and the receiving point 12 was located above the horizontal plane, which was greatly affected by the wall reflection noise and the experimental background noise, so there was an error.

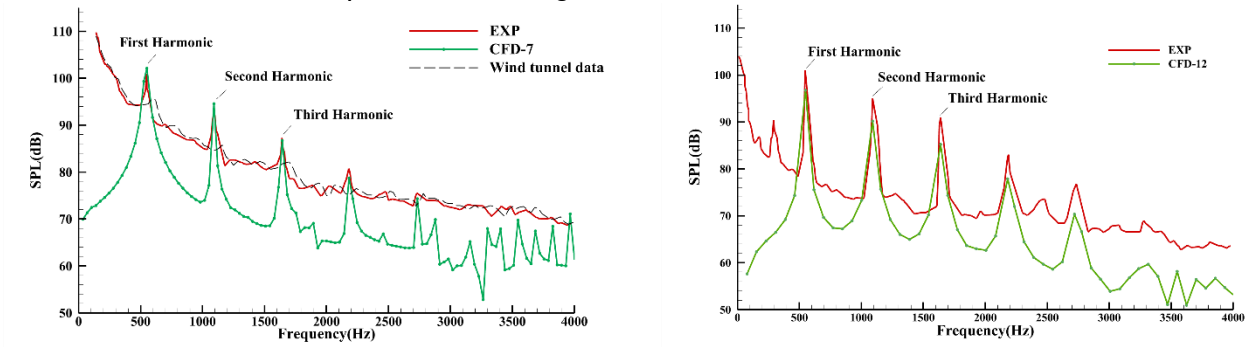

(a) Receiver 7 (b) Receiver 12

Figure 14 – Noise at transducers from a permeable FW-H surface.

2.4 Aerodynamic Performance Prediction of the Isolated Main Rotor and Propellers

For isolated rotors and propellers, Reynolds average N-S equation (RANS) based on steady state flow model with MRF method was used to obtain aerodynamic parameters quickly. The k-ω SST turbulent flow model is adopted which has high simulation accuracy for inverse pressure gradient flow. The aerodynamic performance of rotor and propeller were presented.

2.4.1 Isolated Rotor

The main rotor of X3 helicopter model in this paper is transformed from the main rotor of XH-59A helicopter, where blade number changed into 5. They are rotating anticlockwise from vertical view. The collective pitches of the rotor at 0.75R in range 12~15° were selected for the simulation. The thrust coefficient CT, torque coefficient CQ and Figure of merit FM are calculated according to equation (6~8). Corresponding numerical data are provided in Fig.15.

$$C_T = \frac{T}{\rho \pi R^2 (\Omega R)^2} \tag{6}$$

$$C_Q = \frac{Q}{\rho \pi R^2 (\Omega R)^2 R} \tag{7}$$

$$FM = \frac{C_T^{3/2}}{\sqrt{2} C_Q} \tag{8}$$

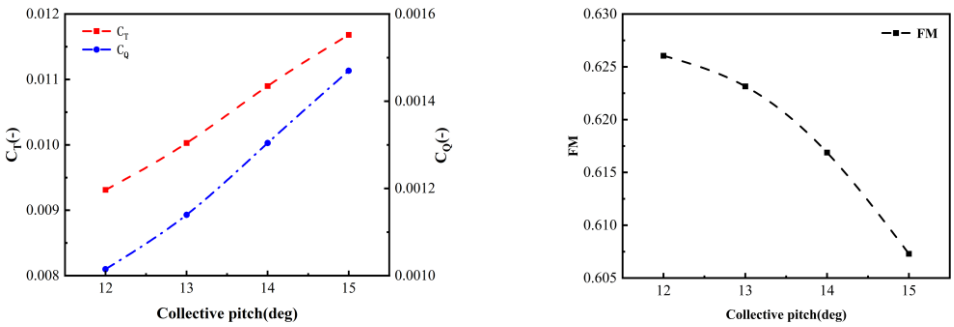

(a) C_T and C_Q varying with collective pitch (b) FM varying with collective pitch

Figure 15 – Aerodynamic performance of isolated main rotor

2.4.2 Isolated propeller

Periodic boundary condition and MRF method are employed for the aerodynamic prediction of the isolated propeller and two sets of grids were used in the propeller model, namely, the rotating domain and the static domain, with total amount of unstructured mesh 3.22 million and 23,000 respectively. Fig. 16 shows the CFD model of the propeller. In the static domain, the radial is 10m and axial is 14m (the wall position is in the middle of the axial position). In the rotating domain, the radial is 2m and axial is 6m. Boundary layer mesh are employed on the surface of the blade with the first layer thickness 3.28×10^{-6}m.

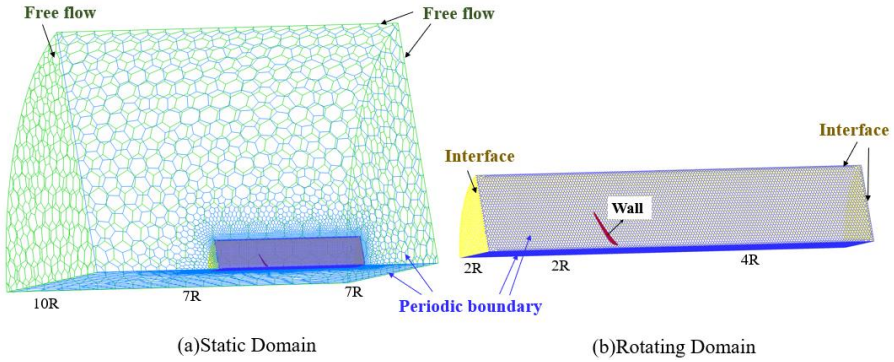

Figure 16 – CFD model for the propeller

Eight simulation models of propeller were created in hover and forward flight to calculate the thrust, torque in collective pitch range 0~20° and -25~-10° for the left and right propeller respectively. And the calculated result are shown in Fig. 17. It is evident from Fig. 17 that the left propeller provides a positive thrust and the right one provides a negative thrust.

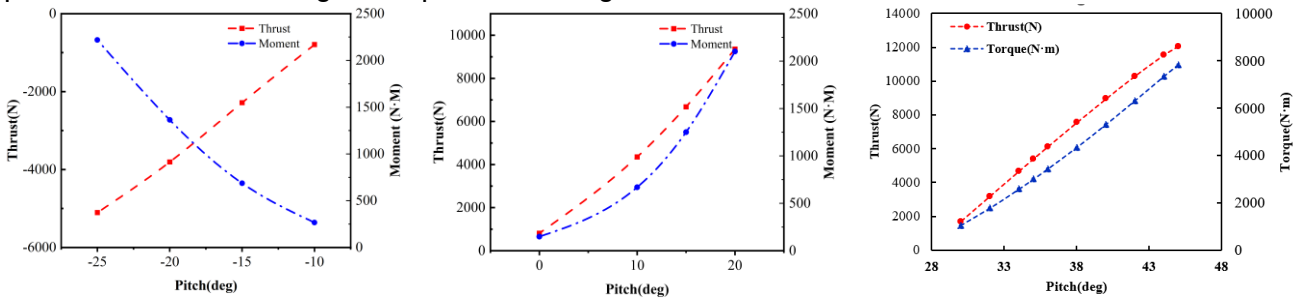

(a) Negative pitch range for left propeller

(b) Positive pitch range for right propeller

(c) Pitch range of forward flight (100m/s)

Figure 17 – Aerodynamic performance of the isolated propellers

3. Determination of Working Parameters Based on the Trim Algorithm

The force and moment of the whole helicopter are in a balanced state in hover. Considering the small attitude angle of the fuselage, the influence between various pneumatic components was temporarily ignored. Assuming that the acting points of each aerodynamic component did not change with the attitude of the helicopter [21], a simplified trim model was established.

3.1 Hover trim

The wing drag and lift were small and could be omitted. Rotor thrust was balanced with the weight of the whole helicopter, and the torque generated by the rotor was balanced by the propellers on both sides of the wing tip, and the rolling moment and pitching moment were automatically balanced by the aileron and the tail elevator. Therefore, the right propeller pulls in the opposite direction to the left propeller in hover. In the case of hover and low speed forward flight, the negative thrust of the right propeller for the balance rotor will produce a large reverse force, and its induced speed is opposite to the direction of the forward flight speed. When the absolute values of the two are close, the right propeller will enter the vortex ring state, and the momentum theory is no longer applicable. In order to avoid this situation, the right pitch Angle should be selected to make the right propeller produce less reverse force when the hover and forward flight speed are small.

Fig. 18 shows the forces and moments acting on the helicopter in the body axis system. Then the

simplified balance equation was as follows:

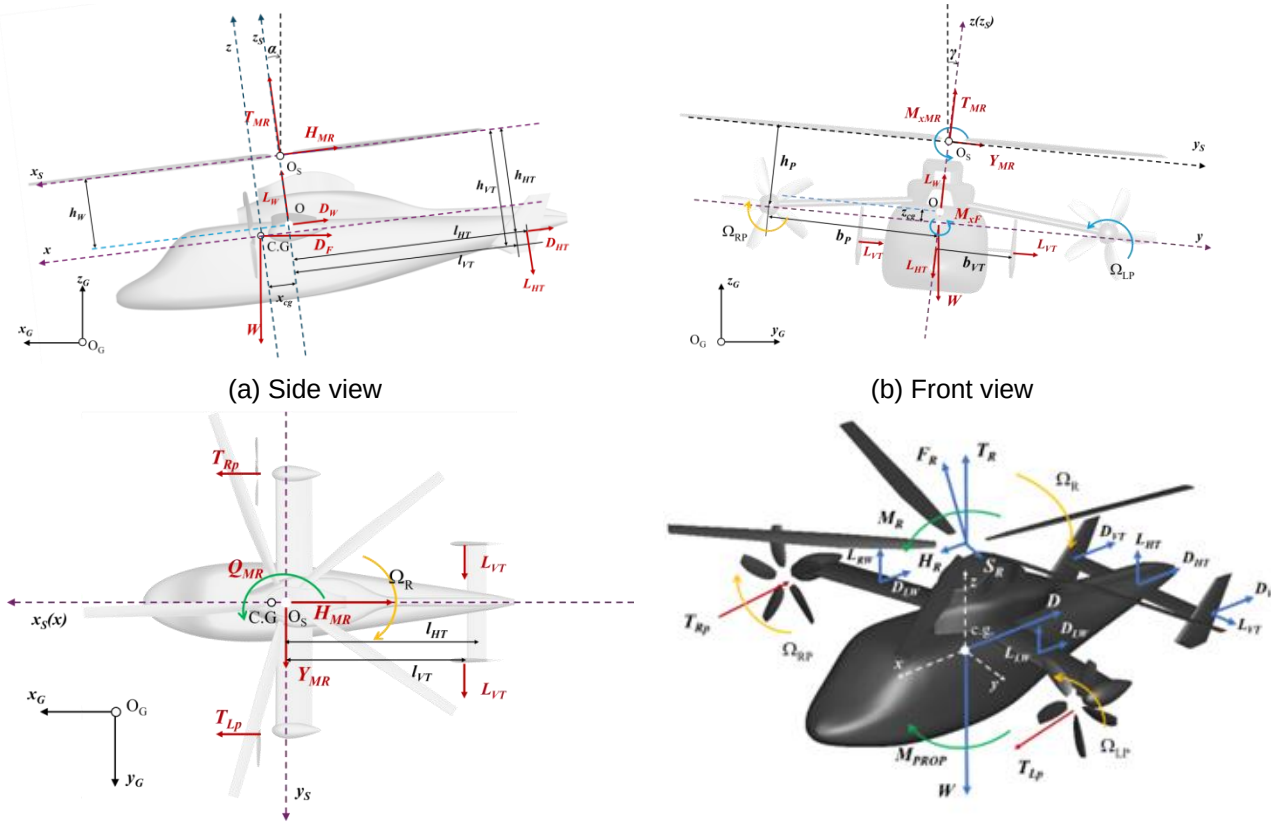

(a) Side view (b) Front view

(c) Top view (d) Forces and moments on the helicopter

Figure 18 – X3 helicopter force diagram

$$Wh_W + (T_{LP} + T_{RP})h_p = 0 \tag{9}$$

$$Wh_F \sin\gamma + Q_{LP} + Q_{RP} = 0 \tag{10}$$

$$Q_{MR} + (T_{LP} + T_{RP})b_p = 0 \tag{11}$$

$$W \sin\alpha + T_{LP} + T_{RP} = 0 \tag{12}$$

$$W \cos\alpha + T_{MR} = 0 \tag{13}$$

According to the above formula, the whole helicopter trim calculation was carried out. After iteration, the final control and attitude parameters in hover were shown in the table 11.

Table 11 –Control and attitude parameters in hover

	Collective pitch of rotor	Pitch of left propeller	Pitch of right propeller	Pitch Angle α/°	Roll Angle γ/°
Parameter	14.00	15.19	-14.58	5.00	-0.25

4. Aerodynamics and Aeroacoustics Characteristics Analysis of the Whole Helicopter in Hover

4.1 Aerodynamic performance

With the collective pitch determined by the trim method for rotor and propellers, the whole flow field across the helicopter is created. Unstructured polyhedral mesh is used. Three rotating zones surrounding the main rotor and helicopters are created with the static zone of the fuselage. For the latter domain, a cylinder with 220m length and 110m radius is applied. Far field boundary condition is applied on the sphere with Ma 0.001. Unsteady flow simulation is carried out using sliding mesh technology. The total numbers of grids are 7.69 million for both propeller domain, 14.64 million for rotor domain, and 13.33 million for static domain. Both the propeller and the rotor area are paddle-tip encrypted. Fig. 18 shows the mesh on the characteristic surfaces. A time step 0.5ms is adopted for the calculation, which is corresponding to rotor rotates 1° and propellers rotates 6° . The

permeable surface is a sphere with a radius 11m from the center of the rotor. The receiving points are a hemispherical sphere with a radius of 22m from the center of the rotor. The spatial discretization third-order MUSCL scheme and the time discretization second-order scheme were used, with 20 internal iterations, and the results were read after 3 rotations of the rotor. The IDDES model was employed.

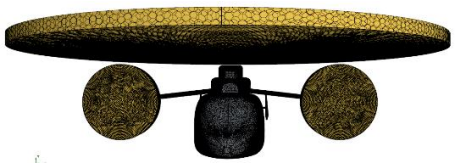

(a)Fuselage and rotation area surface mesh

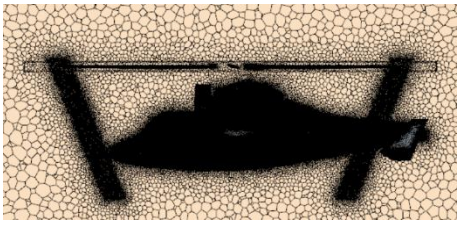

(b)Fuselage, rotor, propeller and symmetry surface mesh

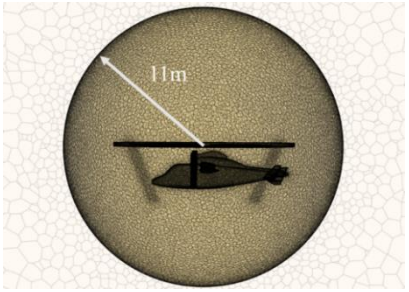

(c) Permeable surface area size and mesh

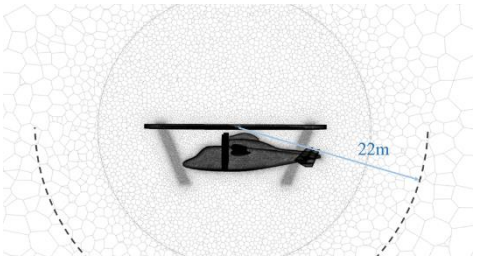

(d) Grid cross-section and receiving point location (y=0)

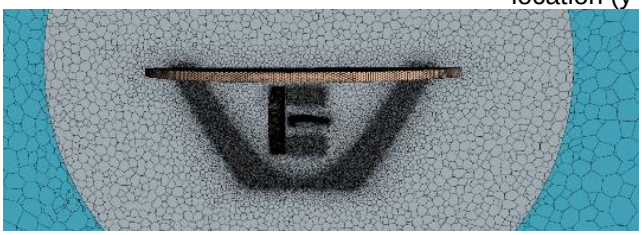

(e)Mesh cross-section (y=3.5)

Figure 19 – Mesh distribution of the whole helicopter model

The aerodynamic performance of rotor, propeller and wing under flow interference are compared with the isolated model in Table 12.

Table 12 – Aerodynamic performance comparison of components between design value and whole helicopter model

Parameter	T_R(N)	Q_R(N·m)	T_{LP}(N)	Q_{LP}(N·m)	T_{RP}(N)	Q_{RP}(N·m)
Isolated	54406.89	31908.79	6575.01	1221.76	2355.88	712.50
Interference	56580.00	34932.90	7288.90	1307.90	2868.29	947.43
Error	3.99%	9.48%	10.86%	7.05%	21.75%	32.97%

As can be seen from Table 12, in the interference state, the aerodynamic force of all components of the helicopter changes significantly. The rotor thrust is increased by 3.99% and the torque is increased by 6.38%. This is because, the rotor part of the downwash flow is blocked by the wing in hover, forming a local high pressure area to increase the thrust and torque. At the same time, the left and right propellers produce the opposite direction of thrust, and the thrust and torque are improved under the interference significantly. This is due to the influence of the downwash flow of the rotor, the blade element angle of attack and the incoming flow velocity of the propeller have changed.

In order to explain the mechanism of flow interaction, the pressure and velocity distribution on the surface of the rotor, propellers and fuselage as well as x=0 plane (central plane of the rotor disc) is investigated. It was found that the pressure range of the whole flow field is -76000Pa~41000Pa, and velocity is 0~500m/s. In order to display the pressure and velocity difference clearly at the sensitive location, the pressure is limited range -500~500Pa, and velocity in range 0~50m/s in Fig. 13. These range were also adopted in the following figures.

In Fig. 20, part of the rotor downwash airflow is blocked by the wing, resulting in irregular flow under the wing. The air flow between the wing and rotor moving from the wingtip to the fuselage gradually,

is blocked and rolled up by the fuselage at the wing root, and sucked in by the rotor, forming circular flow. This phenomenon is known as the *fountain effect*. The slipstream generated by the propeller interferes with the downwash flow of the rotor, which makes the velocity distribution of the downwash flow of the rotor disk asymmetrical, and the slipstream of propellers deflected obviously.

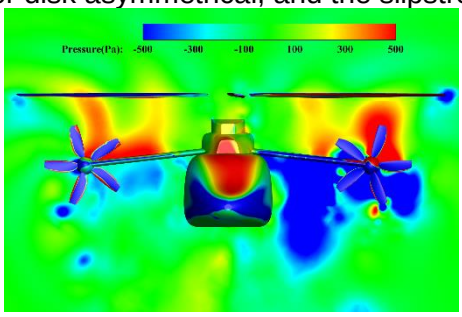

(a) Pressure contour (x=0m plane)

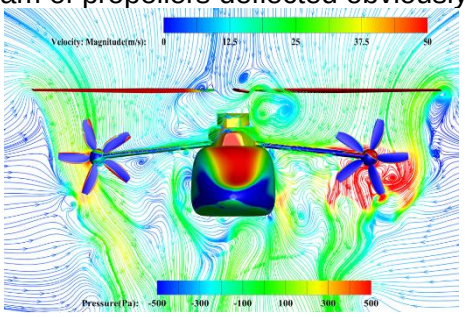

(b) Velocity stream (x=0m plane)

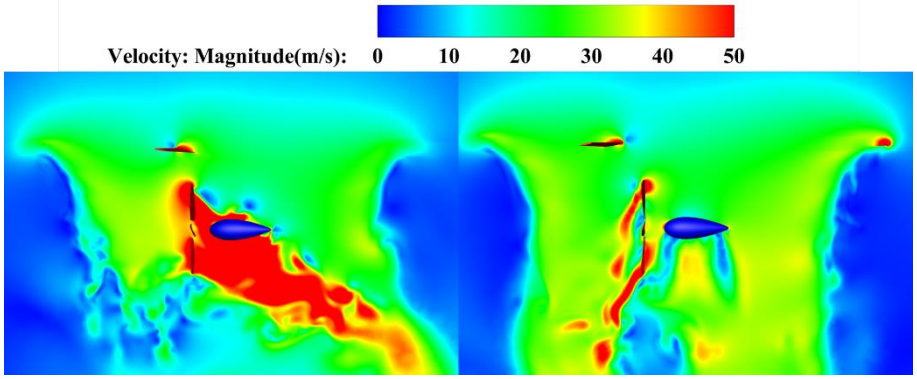

(c) Left propeller (y=3.5m plane) (d) Right propeller (y=-3.5m plane)

Figure 20 – The pressure and velocity contour of the whole helicopter flow model

Note: (b) The middle flow line is dyed by speed, and the body is dyed by pressure

The figure 21 shows a comparison between the vertical velocity distribution contour of the rotor/propeller/wing/fuselage combination and the isolated rotor in the rotor disk section. It can be seen from the figure that when the rotor is isolated, the vertical velocity at the rotor disk is evenly distributed, and the downwash velocity increases first and then decreases along the radial direction, with the maximum downwash velocity between 0.7R and 0.9R. Compared with isolated rotors, the biggest difference in vertical velocity distribution of the rotor/propeller/wing/fuselage combination at the rotor disk is in the root area of the rotor disk. This is due to the serious interference between the rotor and the fuselage and the wing, the circulation flow between the rotor and the wing and the interference between the rotor and the fuselage lead to the change of the vertical velocity distribution of the rotor.

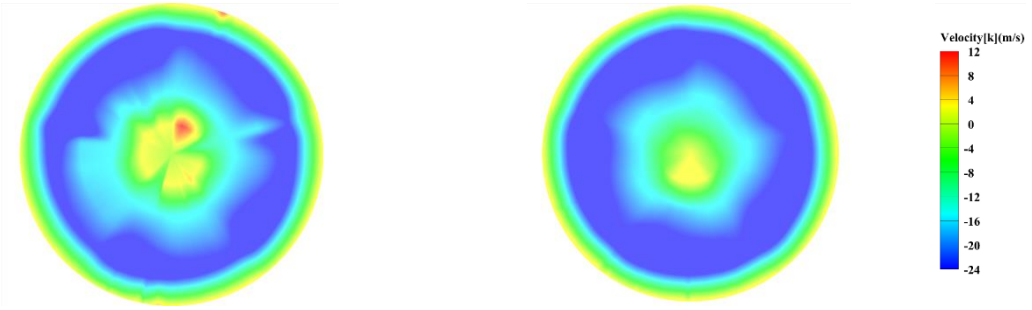

(a) Rotor/propeller/wing/fuselage combination (b) Isolated rotor

Figure 21 – Vertical velocity contour of rotor disk section in hover

FIG. 22 shows the axial induced velocity distribution of the left and right propellers under the condition of full combination and no interference. As can be seen from the figure, in the absence of interference, the axial velocities at the propeller discs of the left and right propellers are evenly distributed, showing a trend of first increasing and then decreasing along the radial direction, and the axial velocities of the left and right propellers are opposite, and the larger axial velocities of the left and right propellers are located between 0.6R and 0.8R. However, the axial speed distribution of the rotor/propeller/wing/fuselage combination at the propeller disk of the left and right propeller moves

down more than that in the condition of no interference, and the maximum speed distribution area is also significantly reduced. This is because there is serious interference in the sliding flow of the left and right propeller under the action of the rotor downwash flow, resulting in changes in the axial speed of the propeller. There's also interference from the wings.

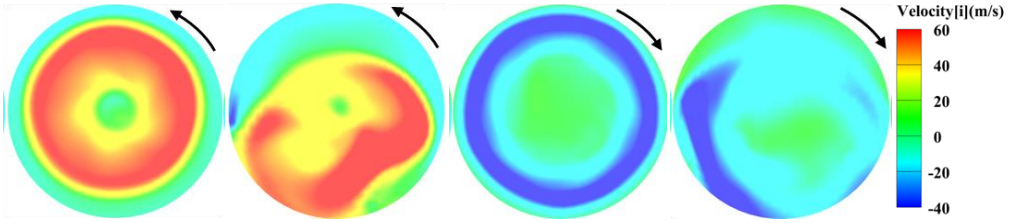

(a) Isolated state and combined state (b) Isolated state and combined state

Figure 22 – Axial velocity distribution of left and right propeller before and after interference

Fig. 23 shows the propeller slipstream passes over the left wing surface due to the forward thrust of the left propeller, resulting in more low pressure areas on the left wing. On the other hand, the right wing was less affected by the propeller slip-stream because the right wing airflow flowed from the trailing edge of the wing to the upper and lower surfaces, and then through the propeller disc. The asymmetric distribution of the pressure on the left and right wings causes the roll torque of the fuselage.

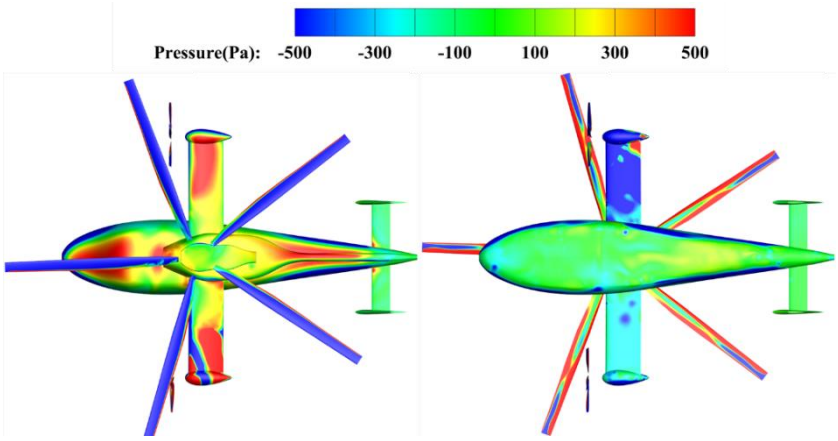

(a) Upper surface (b) Lower surface

Figure 23 – The contour of upper and lower surface

In the figure 24, we can intuitively observe the flow of the rotor downwash flow on the wing surface after it is blocked by the wing. The flow of the left and right wings is not the same. The left wing is affected by both the left propeller slipstream and the rotor downwash, and the airflow accelerates through the propeller, so the velocity is faster at the leading edge of the wing tip. At the same time, under the action of the rotor downwash flow, it flows to the leading edge and the trailing edge of the wing, respectively. On the right wing, there is almost no slipstream interference from the right propeller, so it mainly presents the flow condition formed after the rotor downwash flow is blocked: the air flow flows along the wing spread towards the wing root, and the flow is divided into two parts, one part flows to the leading edge of the wing and the other part flows to the trailing edge of the wing.

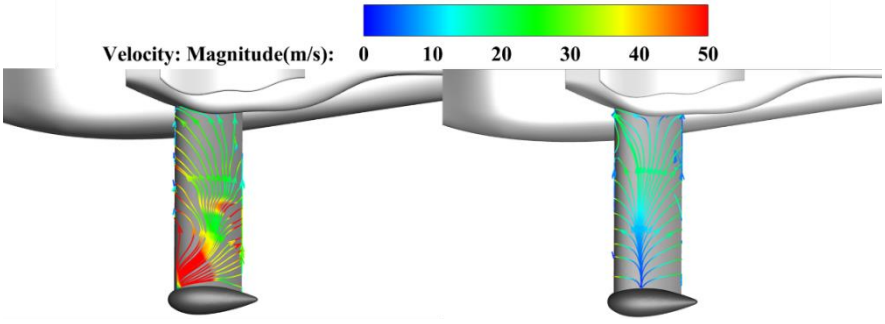

(a) Left wing (b) Right wing

Figure 24 –Left and right wing surface velocity streamlines

Finally, the stress of the wing is obtained as shown in the table 13.

Table 13 –Force comparison between wings

	Left wing	Right wing
Lifting force /N	-3847.78	-1468.86
Drag force /N	1130.25	233.15
Lateral force /N	-592.86	-276.96

As can be seen from the figure 25, on the symmetry plane of the fuselage, the vorticity of the rotor tip falling off will interfere with the tail of the fuselage, especially the position of the vertical tail, and affect the change of the aerodynamic characteristics of the tail. In the left propeller area, the trajectory of tip vortex is obviously deflected under the influence of the rotor, and it can be seen that the tip vortex of the rotor is involved in the left propeller area, causing vortex-vortex interference with the left propeller tip vortex. Due to the influence of the rotor, the trajectory of the tip vortices of the right propeller is also deflected, and some tip vortices that fall off the rotor are involved in the right propeller area, resulting in vortex-vortex interference. These phenomena will cause the acoustic level and distribution to change.

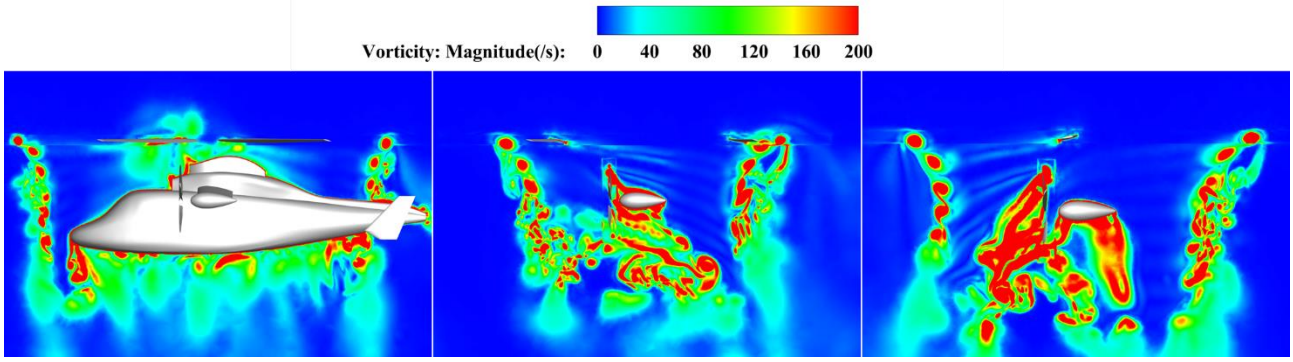

(a)Fuselage symmetry (y=0) (b)Left propeller (y=3.5) (c)Right propeller (y=-3.5)

Figure 25 – Vorticity contour of different cross sections

4.2 Aeroacoustics performance

After the steady flow field of X3 helicopter was obtained in hover according to Section 4.1, the FW-H equation with permeable integral surface was used to predict acoustic in hover state. The physical time starts at 0.6s (three rotations of the rotor) and the maximum physical time is 2.2s (11 rotations of the rotor) for a total of 4,400time steps. In order to display the distribution of the whole helicopter noise during hover better, the rotor rotation center was set as the spherical center, the maximum radius was located in the rotor rotation plane, and the hemispherical surface with a radius of 22m was used as the noise receiving surface. The spherical surface was divided into 12 parts by latitude and 40 parts by longitude, and 480 noise receiving points located on the spherical surface were obtained.

(a)Top view (b)Side view (c)Noise receiving surface

Figure 26 – Receiving point distribution

The figure 27 shows the OASPL distribution in the hovering state of the isolated rotor, double-propeller and rotor propeller wing fuselage combination. The sound pressure level of the isolated rotor is symmetrical in hover, which is mainly composed of load noise and thickness noise. And high Speed Impulsive noise (HSI) is avoided by keeping the blade tip Mach number under 0.85 for all flight conditions. The OASPL of the double-propeller is concentrated in the area near the propeller rotation plane of the left and right propellers, that is, φ=70°~100° and φ=250°~270°. The distribution of higher OASPL is closer to the downstream position of left and right propeller slipstream. At the same time,

because the working state of the right propeller is different from that of the left conventional propeller, the peak value of the OASPL of the right propeller is higher than that of the left. In the combined state, the spatial distribution of sound pressure level changes. Under the combined action of propeller and rotor, the sound pressure level near the left and right propeller sides is obviously higher than other positions. At the same time, the rotor tip vortex that falls off from the rotor interferes with the tail, resulting in a higher noise level in the position of the tail. In addition, due to the vortex-vortex interference between the left and right propeller tip vortexes and the rotor tip vortexes, secondary peaks below the sound pressure level of the propeller region but higher than other regions appear at φ=45° and φ=225°. However, there is also rotor and tail interference at φ=45°, so the distribution range of high sound pressure level here is obviously larger than that at φ=225°.

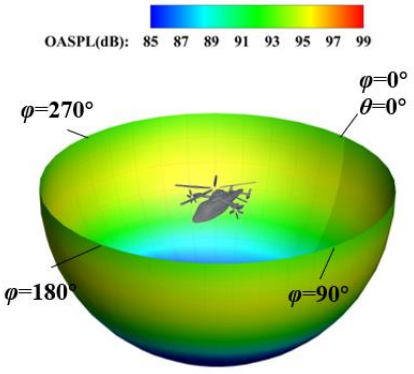

(a) Hemispherical distribution of isolate rotor

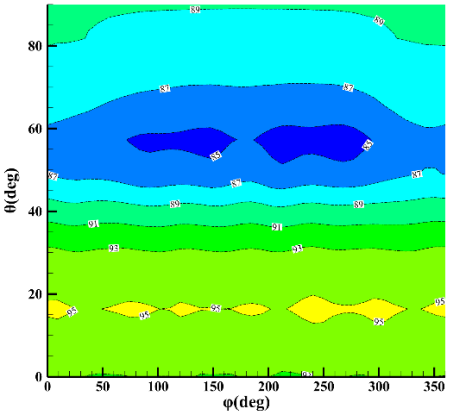

(b) Polar distribution of isolate rotor

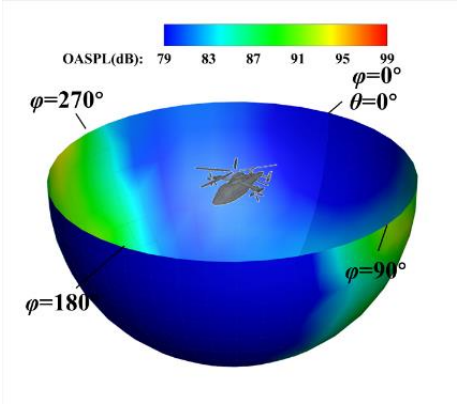

(c) Hemispherical distribution of double-propeller

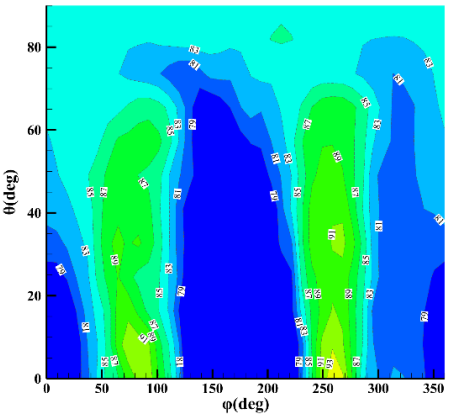

(d) Polar distribution of double-propeller

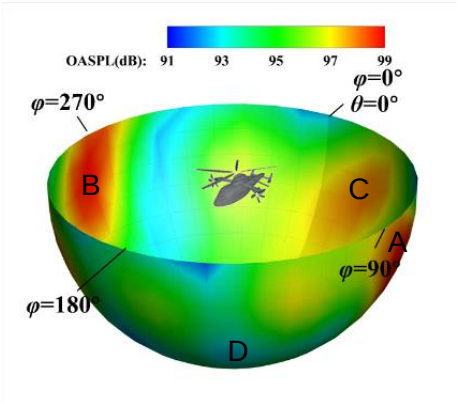

(e) Hemispherical distribution of combined states

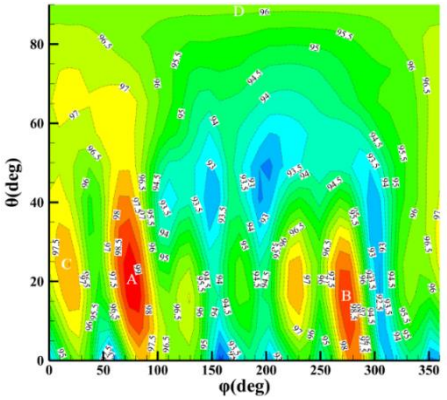

(f) Polar distribution of combined states

Figure 27 – OASPL distribution under different combinations

The regions where the total sound pressure level decreases in order are the left propeller area, the right propeller area, and the rear fuselage and the bottom of the helicopter (θ=90°). In order to better observe the spectrum of high noise points, receiving points A,B,C, and D are selected in the above sound pressure level high level region, as shown in the figure 28 .

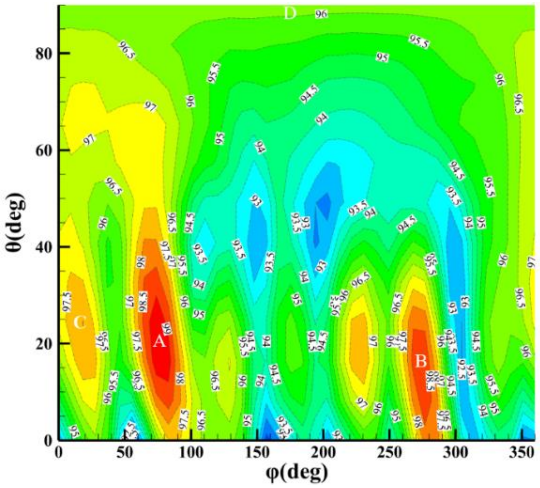

Figure 28 – OASPL plane distribution in the combined state

It can be seen from the figure 29 that at observation points A and B, the fundamental frequency of the rotor and the fundamental frequency of the propeller contribute the most to the total sound pressure level of the point, and the power of the left propeller is higher than that of the right propeller, making the fundamental frequency sound pressure level of the left propeller significantly higher than that of the right propeller. Point C is the rear position of the fuselage. It can be seen from the sound pressure level diagram that the reason for the high total sound pressure level at point C is mainly due to the interference between the rotor and the fuselage, and the vorticity - vorticity interference between the rotor and the left propeller is also a relatively important part. At the bottom of the fuselage, that is, at the D receiving point, it can be obviously observed that the peak value of the base frequency position of the propeller is higher, and compared with the isolated rotor, the sound pressure level at the base frequency of the rotor is also significantly increased due to the interference of the propeller and the rotor. Therefore, the propeller noise mainly radiates as in-plane noise, which means that the noise is greatest directly below the aircraft. And the reason for these phenomena is the propellers operate at higher tip speeds and disk loadings, and they have a lower aspect ratio than the rotor. This design results in higher noise levels from the propellers than from the rotor.

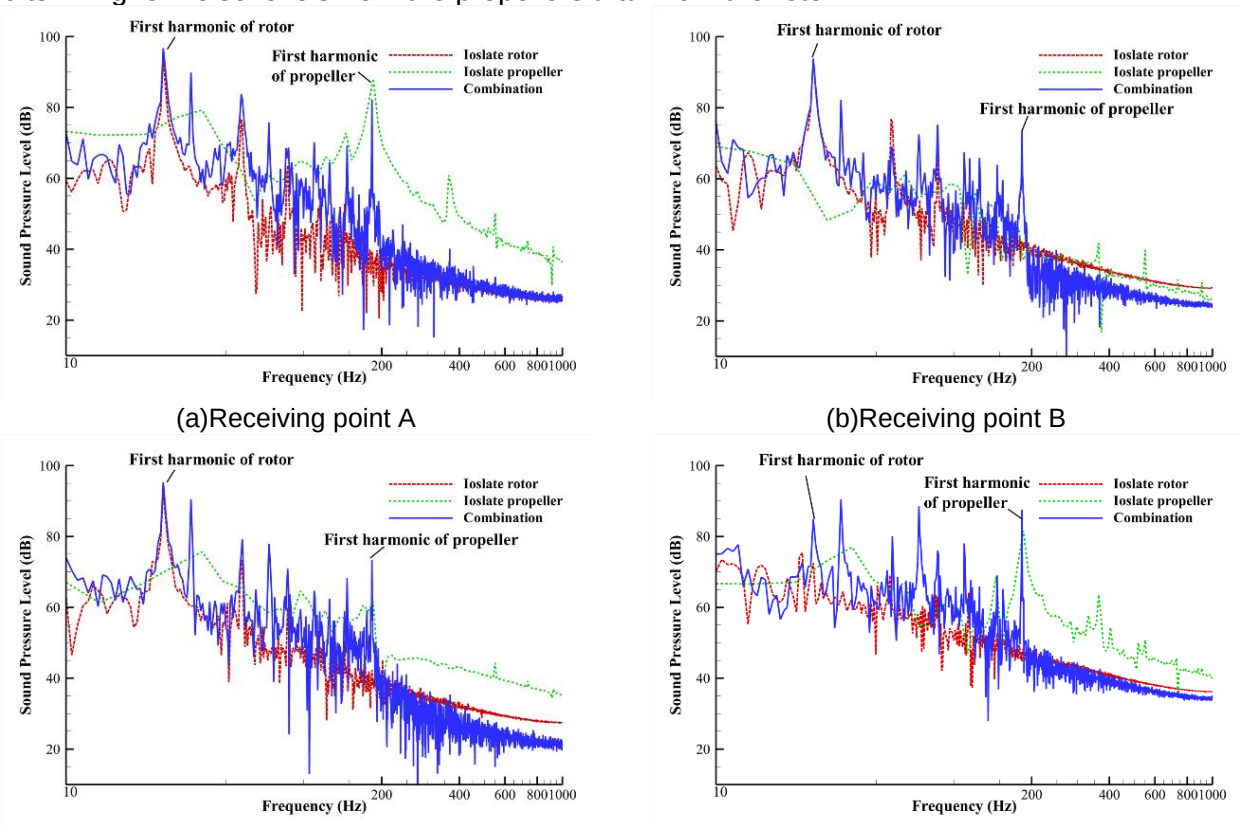

(a)Receiving point A (b)Receiving point B

(c)Receiving point C (d)Receiving point D

Figure 29 – Spectrum diagram of SPL at receiving points

5. Conclusion

In this paper, through the overall parameter design of X3 configuration helicopter, the aerodynamic performance analysis and noise analysis of helicopter rotor, propeller and wing fuselage in hover state are completed. The following conclusions are drawn.

(1) In the case of the overall disturbance of the helicopter, the rotor thrust performance is increased by 3.99%, the torque is increased by 9.48%, and the hover efficiency is reduced by 2.3%. Left propeller thrust increased by nearly 10%, torque increased by nearly 7%; Right propeller thrust increased by 21.75%, torque increased by more than 30%.

(2) Under the interaction of rotor downwash and propeller slipstream, the wing generates negative lift, and the negative lift of the left wing is greater than that of the right wing. At the same time, because the fuselage interferes with the rotor, the vertical velocity of the rotor changes.

(3) The isolated rotor noise distribution is uniform in hover, and it is mainly composed of thickness noise and load noise. In the combined case, the rotor tip vortex interferes with the left and right propellers and the tail, making the rotor noise characteristics change.

(4) Propeller noise has a significant contribution to the whole helicopter noise level in the characteristic area, especially in the area near the left and right propellers and the bottom of the fuselage.

6. Acknowledgments

The research is founded by Northwestern Polytechnical University Basic Research Innovation Ability Project, China Rotorcraft Special Fund No-2023XYZX040402 and CARDC the Key Laboratory of Rotor Aerodynamics Fund No-RAL202303-2.

7. Contact Author Email Address

Mailto: 18183186285@163.com

8. Copyright Statement

References

[1] Chen M., Wu M., Chao F. Technology and Development Overview for Compound Helicopter[J]. Aeronautical Manufacturing Technology,2017,(21),94-101.

[2] Liu Cheng. Research on Preliminary Design of ZF-1 Type High-speed Helicopter[D]. Nanjing: Nanjing University of Aeronautics and Astronautics, 2012.

[3] Zhao Y.Y., Li X., Shi Y. J., et al. Analysis on rotor-propellers interaction flow field for compound double-thust-propeller high-speed helicopters[J]. Journal of Nanjing University of Aeronautics & Astronautics,2017,49(2):154-164.

[4] Whitfield D L. Jameson A. Three-dimensional Euler equation simulation of propeller-wing interaction in transonic low[R]. AIAA Paper83-0286-1983.

[5] Zori L A J. Rajagopalan R G. Navier-Stokes calculations of rotor-airframe interaction in forward flight[J]. Journal of the American Helicopter Society. 1995-40(2):57-67.

[6] Lee B J. Kwon O J. Predicting aerodynamic rotor-fuselage interactions by using unstructured meshes[J]. Tran. Japan Soc. Aero. Space Sci.2002-44(146):208-216.

[7] Chffin M S. Berry J D. Helicopter fuselage aerodynamics under a rotor by Navier-Stokes simulation[J]. Journal of the American Helicopter Society. 1997-42(3):235-243

[8] He CJ, Zhao J G. Modeling rotor wake dynamics with viscous vortex particle method[J]AIAA Journal200947(4):902915.

[9] Wei P, Shi Y J, Xu G. H., et al. Numerical method for simulating rotor flow field based upon viscous vortex model[J]. Acta Aeronautical et Astronautical Sinica,201133(5):771-780

[10]Tan J F, Wang H W. Numerical analysis of helicopter rotor/fuselage unsteady aerodynamic interaction[J]. ACTA Aerodynamical Sinical, 2014，32(3):320 327.

[11]Chen G Q, Bai P, Zhan H L, et al. Numerical Simulation Study on Propeller Slipstream Effect on High Altitude Long Endurance Unmanned Air Vehicle(HALE UAV) [J].Aircraft Design, 2014, 34(4): 19.

[12]Mi B G, Zhan H. Numerical Simulation of the Static and Dynamic Aerodynamics o f a UAV under Wake Flows[J]. Journal of Advanced Transportation,2019,2019:1-12

[13]Felker F F. Performance and Loads Data from a Wind Tunnel Test of a Full-Scale Coaxial Hinge less Rotor Helicopter[R]. NASA-TM-81329,1981.

[14]Johnson W. Lift-Offset Compound Design Back-ground, X2TD, JMR ME1A [R].NASA Ames Research Center,2011.

[15]Stickle, G. W., Characteristics of six propellers including the high-speed range[R]. National Advisory Committee for Aeronautics. Report No.594,1937.

[16]Sivells,J.C., Experimental and calculated characteristics of three wings of NACA 64-210 and 65-210 airfoil sections with and without 2 degree washout[Z].Langley Memorial Aeronautical Laboratory.No.1422,1947.

[17]Wen Q. S., Research on Measurement and Adjustment of Horizontal Tail Mounting Angle of a Helicopter [J]. Proceedings of the 3rd China Aeronautical Science and Technology Conference, 2017.

[18]Ffowcs Williams J E, Hawkings D L. Sound Generated by Turbulence and Surfaces in Arbitrary Motionp[J]. Philosophical Transactions of the Royal Society. 1969，A264(1151) : 321-342.

[19]Raymond E M, Susan A G. Steady and periodic pressure measurements on a generic helicopter fuselage model in the presence of a rotor, NASA-TM-2000-210286[R]. California: NASA, 2000.

[20]Boxwell D A, Yu Y H, Schmitz F H. Hovering impulsive noise: Some measured and calculated results[C]. NACA, Langley Res, Center Helicopter Acoustics, 1978.

[21]P. T. Soderman and W. C. Horne, “Acoustic and Aerodynamic Study of a PusherPropeller Aircraft Model,” NASA TP 3040, 1990.

[22]Wang Q. N. Analysis of aerodynamic interference characteristics of high speed helicopter with compound thrust[D]. Nanjing: Nanjing University of Aeronautics and As-tronautics，2021.